

SCIENTIFIC REPORTS



OPEN

Magnetoresistance and robust resistivity plateau in MoAs_2

Jialu Wang, Lin Li, Wei You, Tingting Wang, Chao Cao, Jianhui Dai & Yuke Li

We have grown the MoAs_2 single crystal which crystallizes in a monoclinic structure with $C2/m$ space group. Transport measurements show that MoAs_2 displays a metallic behavior at zero field and undergoes a metal-to-semiconductor crossover at low temperatures when the applied magnetic field is over 5 T. A robust resistivity plateau appears below 18 K and persists for the field up to 9 T. A large positive magnetoresistance (MR), reaching about 2600% at 2 K and 9 T, is observed when the field is perpendicular to the current. The MR becomes negative below 40 K when the field is rotated to be parallel to the current. The Hall resistivity shows the non-linear field-dependence below 70 K. The analysis using two-band model indicates a compensated electron-hole carrier density at low temperatures. A combination of the breakdown of Kohler's rule, the abnormal drop and the cross point in Hall data implies that a possible Lifshitz transition has occurred between 30 K and 60 K, likely driving the compensated electron-hole density, the large MR as well as the metal-semiconductor transition in MoAs_2 . Our results indicate that the family of centrosymmetric transition-metal dipnictides has rich transport behavior which can in general exhibit variable metallic and topological features.

Three-dimensional (3D) topological quantum materials, including topological insulators (TIs)¹, topological Dirac semimetals (DSMs)^{2–6} and Weyl semimetals (WSMs)^{7–14}, have been discovered and intensively investigated recently. These materials exhibit a variety of interesting physical properties, owing to their unique electronic structures and spin textures^{2,6,8,10,15}, and thus show a broad application potential. An ideal TI usually exhibits a clear resistivity plateau at low temperatures due to the robust surface states^{16–19}. In an ideal WSM, the Weyl fermions disperse linearly all the way across the Weyl nodes which appear in pairs with opposite chiralities by breaking time reversal symmetry (TRS) or inversion symmetry^{15,20,21}. The relativistic electronic dispersion and chirality-based topological property result in various semi-metallic transport properties and produce a number of novel phenomena such as the anomalous Hall effect⁷ and the Fermi arcs⁹.

Recently, the WSMs have been theoretically predicted and experimentally discovered in a family of transition-metal pnictides represented by TaAs family^{7–15}. Consequently, dozens of topological semimetals showing exotic physical properties were reported and studied in detail, such as $\text{ZrSiS}(\text{Te})$ ^{22,23}, MoTe_2 ^{24,25} and WTe_2 ²⁶, in addition to the TaAs family. All these materials are non-centrosymmetric in the crystal structure and are further classified into two types of Weyl fermions: with or without the Lorentz symmetry in their energy-momentum dispersions. More recently, a new family of topological semimetals (TSMs) which crystallizes in the centro-symmetry monoclinic structure, the transition-metal dipnictides $X\text{Pn}_2$ ($X = \text{Ta}, \text{Nb}, \text{Pn} = \text{P}, \text{As}, \text{Sb}$) as represented by TaSb_2 , have been discovered^{27–29}.

The reported transport properties of the centrosymmetric $X\text{Pn}_2$ exhibit the extremely large magnetoresistance (MR) and ultrahigh electronic mobility in common^{30–33}. Meanwhile they also exhibit the material's-dependent low-temperatures resistivity plateau and negative MR^{27,30,34}. While the explanations of these features are still complicated, they are likely related to the disentangled bulk electron/hole bands and topological non-trivial surface states as revealed in the electronic band structure calculations³⁵. On the other hand, the coexistence of bulk and surface states is appealing for materials applications. We are thus motivated to search for other candidates in this family with potentially more robust surface states and better metallicity.

In this paper, we report a new member of this family, MoAs_2 , which also crystallizes in a monoclinic structure. Our experimental results indicate that MoAs_2 undergoes a metal-to-semiconductor crossover under the applied magnetic field up to 5 T. In particular, a very clear resistivity plateau is observed below 18 K even in the absence of the magnetic field. The plateau feature is robust against the applied magnetic fields up to 9 T. The MR is relatively large as the applied magnetic field is perpendicular to the current, reaching about 2600% at

Department of Physics and Hangzhou Key Laboratory of Quantum Matter, Hangzhou Normal University, Hangzhou, 310036, China. Correspondence and requests for materials should be addressed to J.D. (email: daijh@hznu.edu.cn) or Y.L. (email: yklee@hznu.edu.cn)

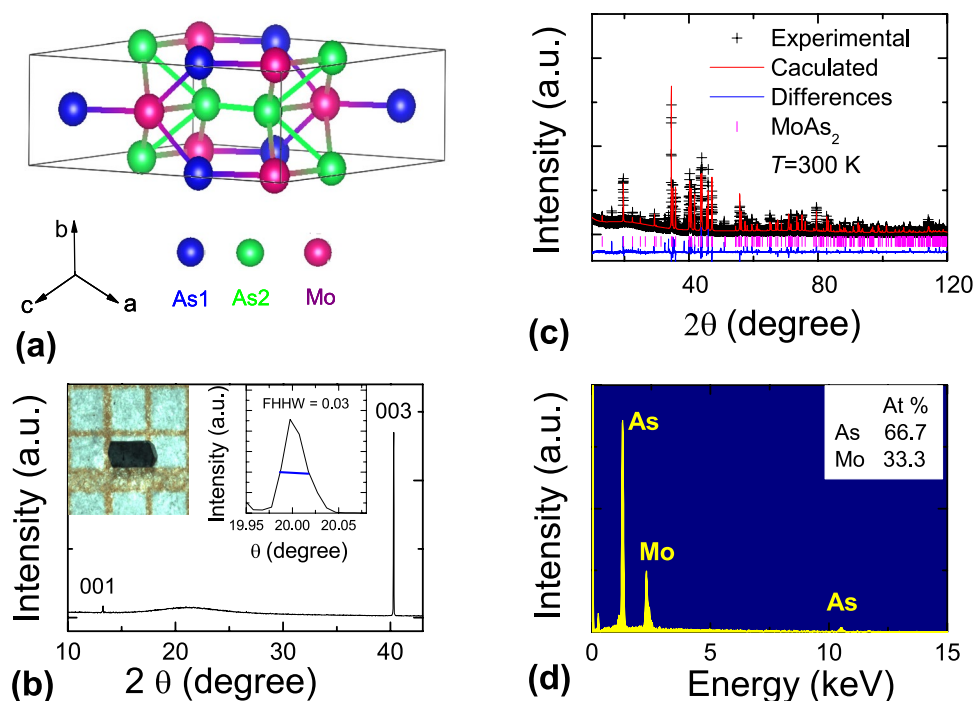


Figure 1. Crystal Structure. (a) The crystal structure of MoAs_2 . (b) The (001) X-ray diffraction patterns of single crystal. Left inset: picture of a typical MoAs_2 single crystal. Right inset: the rocking curve with a very small half-high-width. (c) The Rietveld refinement profile for MoAs_2 sample at room temperature. (d) EDX spectroscopy at room temperature.

2 K and 9 T, but violates the Kohler's rule below 70 K. When the applied field is rotated from perpendicular to parallel to the current direction, the MR drops rapidly and finally becomes negative. Hall resistivity shows the non-linear field-dependence below 70 K and changes from positive to negative at around 40 K. The two-band model fit yields the abnormal drop in hole-mobility below 30 K and a strange cross point in carrier density at around 60 K. All our experimental results indicate a possible Lifshitz transition occurring between 30 K and 60 K, which is likely a direct factor to drive the compensated electron-hole carrier density, the large MR as well as the metal-semiconductor-like transition in MoAs_2 .

Results

Figure 1 shows the detailed information of MoAs_2 crystal structure. In Fig. 1a, MoAs_2 crystallizes in a monoclinic structure with $C2/m$ space group, which is common to the XPn_2 family. Figure 1b shows the (001) peaks of MoAs_2 single crystal X-ray diffraction, implying that the crystal surface is normal to the c-axis. The b-axis is perpendicular to the ac-plane, and parallel to the current direction. The left inset of Fig. 1b shows a picture of a large polyhedral MoAs_2 crystal with millimeter dimension. The polyhedral crystal with rectangle-shape is consistent with the monoclinic structure. The right inset shows the X-ray rocking curve with a very small half-high-width, implying the high quality crystal. Figure 1c exhibits the Rietveld refinement profile and its structure parameters in MoAs_2 at room temperature (more details of crystal structure parameters can be found in Table S1 in Supplementary Information). Through the Rietveld structural analysis, the refined lattice parameters are extracted to be $a = 9.064(7) \text{ \AA}$, $b = 3.298(7) \text{ \AA}$, $c = 7.718(3) \text{ \AA}$, and $\beta = 119.37(1)^\circ$ as reported in the previous literatures^{36,37}. Figure 1d shows the EDX data with the Mo and As contents of 33.3% and 66.7%, respectively, consistent with the ratio of Mo and As.

Figure 2 displays the evolution of the magneto-resistivity as a function of temperature in MoAs_2 down to 2 K with the magnetic field $\mathbf{B} \parallel \mathbf{c} \perp \mathbf{I}$. As shown in Fig. 2a, the value of ρ_{xx} at 300 K is about $163 \mu\Omega \text{ cm}$ at $\mathbf{B} = 0 \text{ T}$, comparable to that of high quality WTe_2 ²⁶ and MoTe_2 ²⁴, the potential candidates of the type-II WSM. While, ρ_{xx} at 2 K falls to $0.29 \mu\Omega \text{ cm}$, yielding a large value of residual resistivity ratio (RRR) = 562. This confirms the high quality of the crystal. The extraordinarily low residual resistivity at 2 K was previously found in Cd_3As_2 ³⁸, ZrSiS ³⁹ and high purity Bi ⁴⁰ with very large RRR.

The zero field resistivity ρ_{xx} exhibits highly metallic behavior. Upon decreasing temperature, it decreases almost linearly in the high temperature regime. Below 30 K, however, ρ_{xx} deviates severely from the Fermi liquid behavior. Considering that this contribution to resistivity involves the electron-phonon(e-ph) interaction according to the Bloch-Gruneisen theory⁴¹. We employed the formula $\rho = \rho_0 + aT^2 + bT^5$ to fit the low temperature resistivity as shown in inset of Fig. 2a, where the ρ_0 is the residual resistivity at $T = 0 \text{ K}$, the terms of T^2 and T^5 represent the contributions of the e-e and e-ph scatter, respectively. It is found that resistivity does not exactly match this fit. Instead it remains almost constant below 20 K, displaying a clear resistivity plateau.

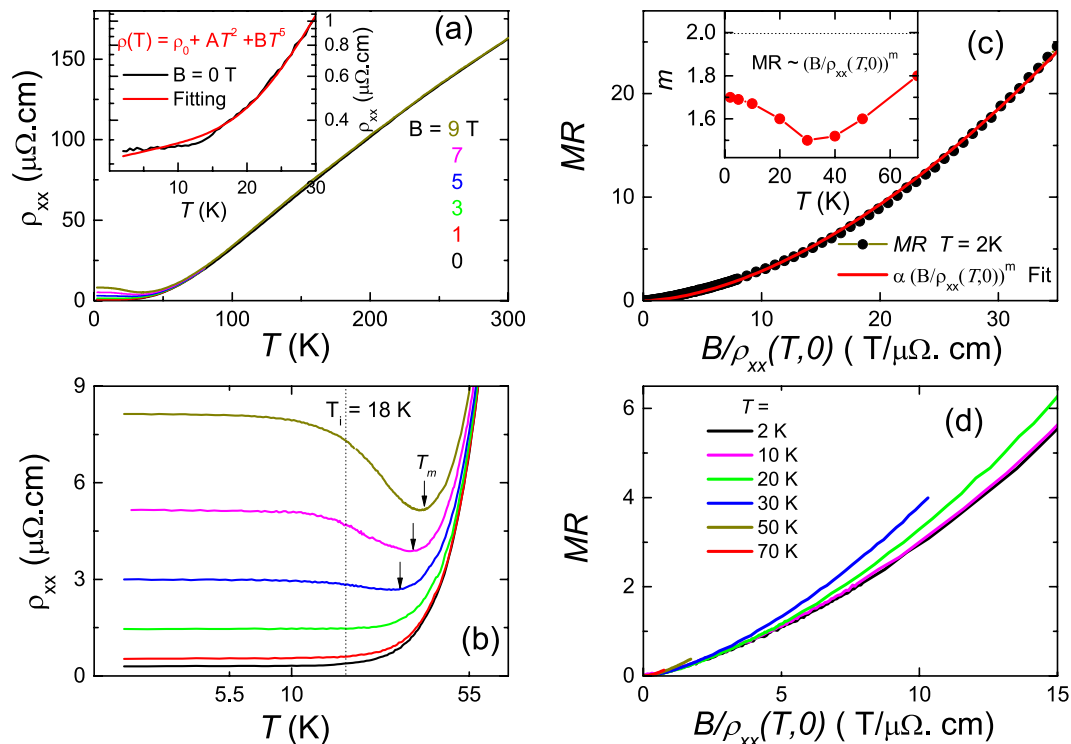


Figure 2. Temperature dependence of resistivity for MoAs₂ and the Kohler's rule below 70 K. **(a)** Resistivity of MoAs₂ as a function of temperature in several magnetic fields ($B = 1, 3, 5, 7, 9$ T) perpendicular to the current. Inset shows a deviated Fermi liquid behavior below 30 K at $B = 0$. The **(b)** shows a clear plateau resistivity at low temperature. **(c)** MR vs. B/ρ_0 at 2 K. The red line represents the fitting curve. The inset shows the fitting m values at different temperatures. **(d)** The breakdown of Kohler's rule below 70 K.

An applied magnetic field does hardly change the resistivity in the high temperature regime as compared with that of the zero field. A significant change in ρ_{xx} appears around $T_m = 40$ K, where the resistivity starts to saturate for small field or crossovers to the semiconductor behavior for large field. After the crossover the resistivity is soon saturated, developing a robust resistivity plateau in the low temperature regime below $T_i = 18$ K, defined as the onset temperature of the plateau where $\partial^2 \rho(T)/\partial T^2 = 0$, as clearly observed in the Fig. 2b. The crossover behavior becomes prominent with increasing magnetic field up to 9 T while the crossover temperature does not change too much.

A large MR ($= (\rho_{xx}(B) - \rho_{xx}(0))/\rho_{xx}(0)$) is observed, reaching 2600% at 2 K and 9 T in Fig. 2c. Although the MR in MoAs₂ is one or two orders of magnitude smaller than that in other semimetal compounds, it is still far larger than the value in some ferrimagnetic materials⁴². According to the Kohler's rule^{41,43} ($MR \propto (B/\rho(T, 0))^m$), all the MR at various temperatures can be scaled onto a single line with a constant $m = 1, 2$. In Fig. 2c, the fit of MR curve at 2 K yields $m = 1.7$. A careful analysis to the MR across the metal-semiconductor-like transition regime found that the m , as shown in inset of Fig. 2c, displays a minimum value around 40 K for $m = 1.5$, but then increases slightly to about 1.7 below 10 K. The small m value substantially violates the classically field-square dependence of the MR in the semiconductor-like regime. Noted that the exponent m (~ 1.5) has been observed in under-doped cuprates and organic conductor which both are widely considered as non-Fermi liquid system^{44,45}. The results, as plotted in Fig. 2d, display that the MR below 70 K obviously deviates from the Kohler's rule, indicating that the sample is a multi-band system possessing the variable carrier concentrations or the mobility ratio of electron to hole when temperature goes down. Therefore, we suggest that the conventional e-e and e-ph interactions may be hard to explain the appearance of resistivity plateau in MoAs₂, implying that this intrinsic plateau is closely related to the topological nature as observed in many semimetal materials^{27,46}.

However, in these semimetal compounds, saturated resistivity plateaus at much lower temperatures are naturally expected. The microscopic origin of this phenomenon remains debated, depending on the expanded energy scale around which the plateau feature sets in. In the candidates of TIs, SmB₆^{18,19} and LaSb^{46,47}, the resistivity plateau is well-attributed to the topological non-trivial surface states which are robust against disorders. It is interesting that a clear resistivity plateau was also observed in TaSb₂, a candidate of TSM²⁷. Although bulk excitations are involved in this material, the resistivity plateau is plausible due to the surface states which are topological non-trivial in the sense of doped weak TIs³⁵. It is remarkable that the resistivity plateau of MoAs₂ sets in at $T_i = 18$ K, about four times of that of SmB₆ ($T = 5$ K)¹⁹.

Now we turn to the MR of MoAs₂ as shown in Fig. 3. All data here are displayed without a symmetrizing process. In Fig. 3a, a large MR at low temperatures is observed when the field is perpendicular to the current direction. The value of MR does not change significantly until 20 K where it decreases sharply in consistent with the robust resistivity plateau which persists up to 9 T. At fixed temperatures, the MR increases quadratically for

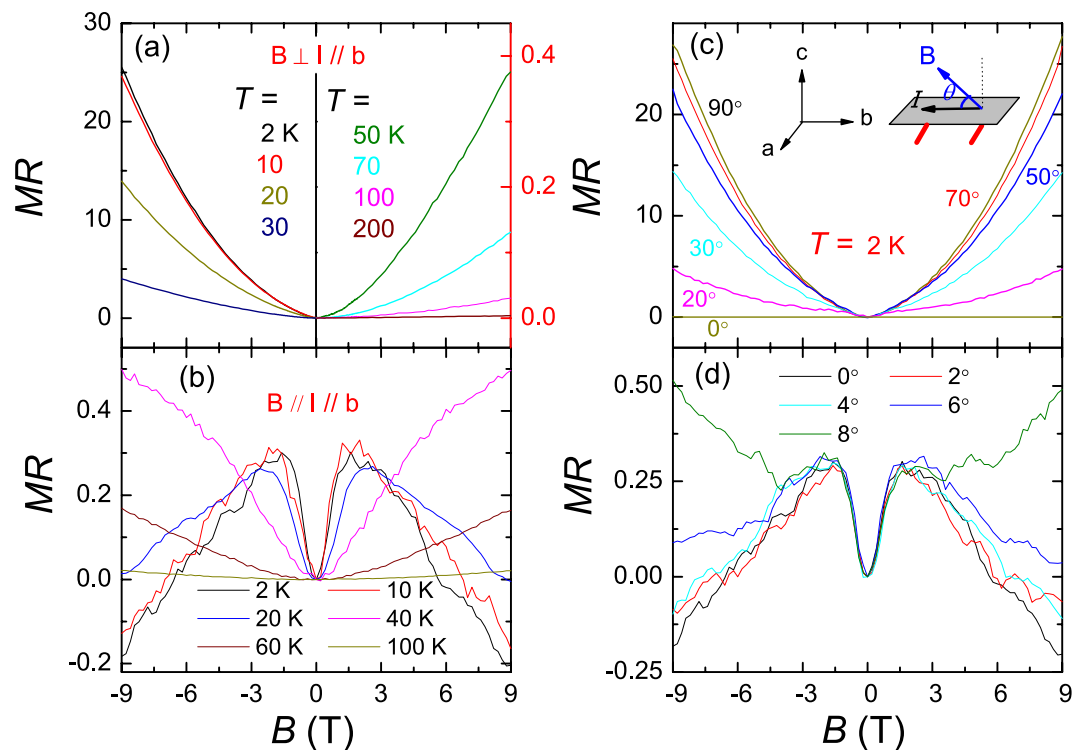


Figure 3. Magnetic field dependence of MR in MoAs₂ single crystal. (a) Magnetoresistance $MR = (\rho_{xx}(H) - \rho_{xx}(0))/\rho_{xx}(0)$ versus magnetic fields along the *c*-axis at different temperatures as $\mathbf{B} \perp \mathbf{I} // \mathbf{b}$. (b) MR vs. fields for $\mathbf{B} // \mathbf{I} // \mathbf{b}$. (c) MR plotted as a function of magnetic fields at different angles between \mathbf{B} and \mathbf{I} . (d) The large and unsaturated negative MR emerges in a narrow window of angle around $\theta = 0^\circ$.

low field and almost linear for larger field without saturation, similar to the previously-known semimetallic materials including TaAs(P)^{7,14}, NbAs(P)^{7,14} and WTe₂²⁶. Further increasing temperature, its value approaches to 3% at 100 K, and is less than 1% above 200 K at 9 T. This feature is in contrast to the most of semimetals with a relatively large MR even at room temperatures^{14,22}.

As the magnetic field is applied along the current direction, $\mathbf{B} // \mathbf{I}$, the MR becomes negative at low temperatures shown in Fig. 3b. These MR curves are overall axial-symmetric around $B = 0$ T, with only slight noises due to the extraordinarily low resistivity. The absolute value of MR is much smaller than that in the case of $\mathbf{B} \perp \mathbf{I}$. At 2 K, the MR first increases until about 2 T, then decreases monotonously with the field and changes a sign from positive to negative as $B \sim 6.5$ T, reaching about 20% at 9 T. The negative MR decreases gradually upon heating and disappears above 40 K, beyond which the MR turns back to positive.

Figure 3c shows the field dependence of MR at various angles θ of the magnetic field with respect to the current direction at 2 K. By rotating $\theta = 90^\circ \rightarrow 0^\circ$, the MR drops quickly and shows quadratically field-dependence. The negative MR is further illustrated in Fig. 3d when θ approaches to 0° . At $B = 9$ T, the MR is still negative for $\theta \leq 4^\circ$. When θ is larger than 4° , the MR recovers positive and increases with θ . The negative MR at $\theta = 0^\circ$ is limited in a narrow window over ~ 6.5 T. The phenomenon of negative MR has been observed in a number of metallic compounds with high mobility of charge carriers. The interpretation of this phenomenon remains debated, too, given the fact that it may appear in both topological trivial and non-trivial materials. A crucial issue behind the negative MR is the current jetting effect due to the field-induced anisotropy. This effect is usually elusive but has been recently suggested as a main cause of negative MR in TaP compound^{14,48}. In the TaSb₂ samples, however, the current jetting effect was shown to play a minor influence on the negative MR by using different contact configurations²⁷. In the ideal WSMs, the negative MR could be best-understood due to the chiral anomaly. The similar topological interpretation applies to those with ill-defined Weyl points or Dirac points if they appear in pairs and separate in momentum space^{49,50}. In the present compound MoAs₂, the topological interpretation seems to be consistent with the robust resistivity plateau discussed previously.

Figure 4 shows the band structure with inclusion of spin-orbit coupling (SOC). The inversive bands from X_1 to Y lead to a Dirac cone in the absence of the SOC, while it opens a gap when the SOC is taken into account, resulting in two disentangled and nearly compensated electron/hole bands. We can calculate the topological index for each of these bands according to the parity-check method⁵¹. Different to TaSb₂ or other previously-known XPn_2 compounds, the indices of the partially-filled bands of MoAs₂ are topologically strong (Detailed analyses for the topological nature of the band structure and surface states will be given elsewhere). The result indicates that the surface states in MoAs₂ are more robust than those in TaSb₂²⁷, consistent with the observed resistivity plateau in our present sample.

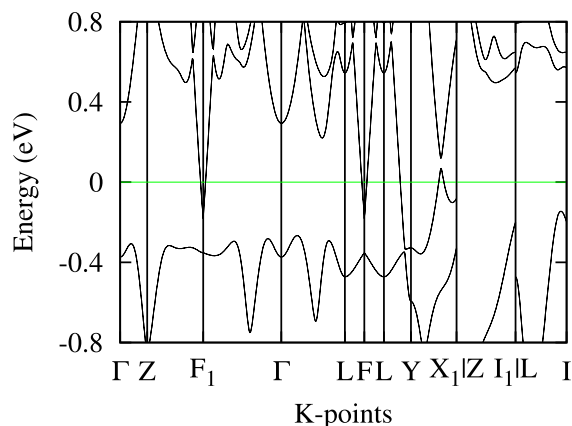


Figure 4. Band structure of MoAs₂ with SOC.

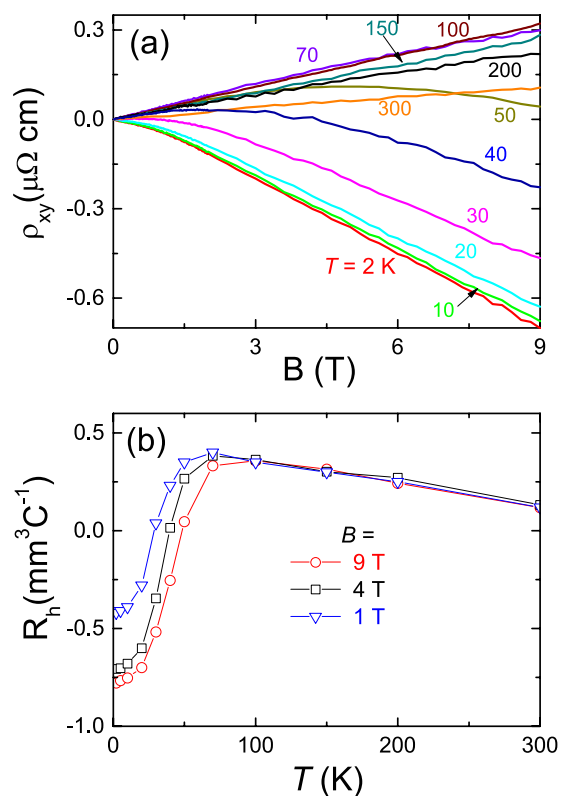


Figure 5. Hall effect for MoAs₂. (a) Magnetic field dependence of Hall resistivity at several different temperatures up to 9 T. (b) Hall coefficient vs. temperatures at 1 T, 4 T and 9 T.

Figure 5a maps the magnetic field dependence of the Hall resistivity for MoAs₂ at various temperatures, with the magnetic field ranging from 0 to 9 T. The field dependence of $\rho_{xy}(B)$ is almost linear with positive slope at high temperature. It starts to bend strongly below 70 K. For $T \leq 40$ K, $\rho_{xy}(B)$ shows a pronounced sign reversal from positive to negative, and finally recovers the nearly linear behavior, implying a multi-band system in MoAs₂. Figure 5b shows the temperature dependence of the Hall coefficient at 1 T, 4 T, and 9 T. As temperature decreases, R_H firstly increases from 300 K, and then undergoes a sharp drop at around 70 K. R_H changes its sign from positive to negative at around 40 K, implying a partial compensation between the hole-type and electron-type carriers at low temperatures. The sign-change in R_H is usually (though not always) an important indication of multiple bands, so the feature of the sign-changed R_H confirms further the multi-band effect in MoAs₂. The sign-changed R_H together with the increase of electron-mobility and -density as shown in Fig. 6 implies a possible temperature-induced Lifshitz transition occurring at around temperature, resulting in a drop R_H below 70 K associated with the decrease of hole pockets.

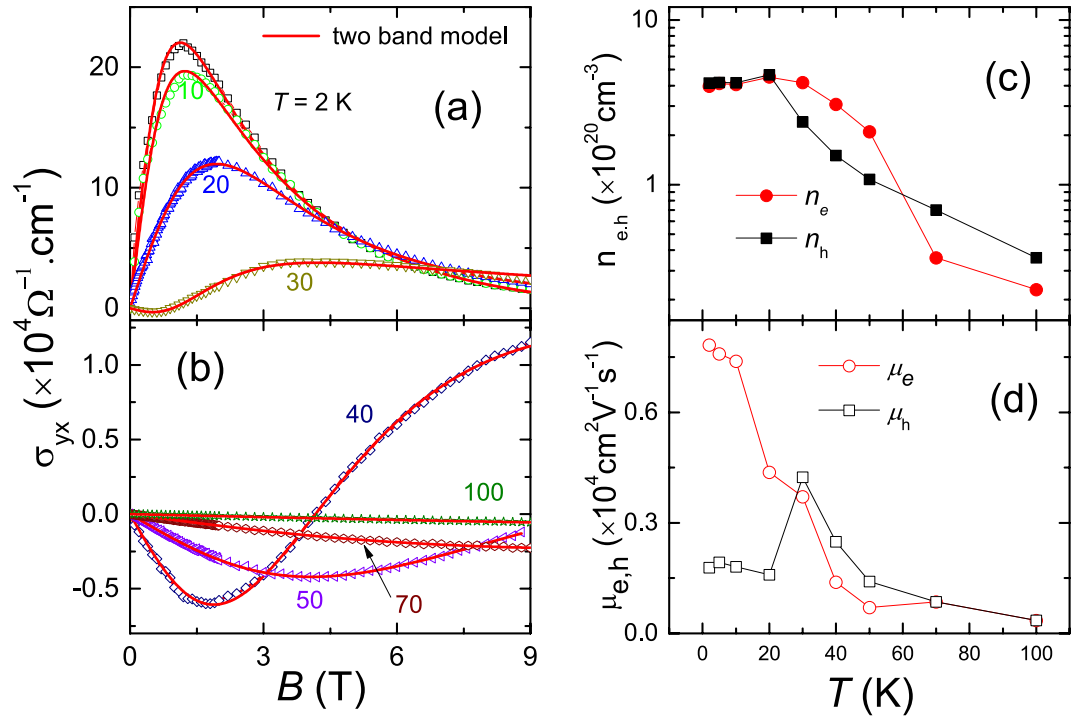


Figure 6. Hall conductivity, the carrier density and mobility. (a) and (b) Magnetic field dependence of Hall conductivity at several representative temperatures up to 9 T. The red solid lines are the fitting curves using two-band model. (c) Electrons and holes densities and (d) mobilities as a function of temperature below 100 K.

We carefully analyze the Hall conductivity according to the two-band model⁴¹. The results of the densities and mobilities of both electrons and holes as a function of the temperature are shown in Fig. 6. In this model, the Hall conductivity tensor is given by:

$$\sigma_{xy} = -\frac{\rho_{xy}}{\rho_{xx}^2 + \rho_{xy}^2} \quad \sigma_{xy} = eB \left[\frac{n_h \mu_h^2}{1 + (\mu_h B)^2} - \frac{n_e \mu_e^2}{1 + (\mu_e B)^2} \right] \quad (1)$$

Here, n_e (n_h) and μ_e (μ_h) are electrons (holes) carrier densities and mobilities, respectively. The result gives an excellent fit below 100 K and the obtained $n_{e,h}$ and $\mu_{e,h}$ as a function of temperature are shown in Fig. 6c and d. Above 70 K, the hole-type carrier dominates, consistent with the positive Hall coefficients as shown in Fig. 5b. With lowering temperature, the electron-type carrier density increases sharply and becomes dominant, resulting in an observed cross point at about 60 K which is very closed to the characteristic temperature (T_m) with the sign-changed R_H . As further cooling down temperature, the $n_{e,h}$ increases slowly, and then becomes almost equivalent and saturated. The calculated density of electrons and holes at 2 K is $3.95 \times 10^{20} \text{cm}^{-3}$ and $4.13 \times 10^{20} \text{cm}^{-3}$, respectively, implying a perfect compensation of semimetal in MoAs₂. In Fig. 6d, the mobility, $\mu_{e,h}$, as a function of temperature increases slightly and displays more or less overlap above 30 K, followed by a huge divergency that μ_h drops suddenly and μ_e increases sharply. Noted that the metal-semiconductor transition occurs at around 40 K, below which the MR starts to increase dramatically. A combination of the drop in mobility, the cross point in $n_{e,h}$ and the sign-changed R_H points to a possible electronic structure change at around 30–60 K, named a Lifshitz transition, directly driving the compensation of electron-hole carriers density at low temperature and the extremely large MR as well. The similar behavior has been investigated in the discovered WTe₂ and MoTe₂ semimetals by the measurement of ARPES^{52,53}, Ultrafast transient reflectivity⁵⁴ and Hall effect^{55,56}.

Therefore, the possible Lifshitz transition can be suggested in MoAs₂, which directly derives a compensated electron-hole carriers density, the large MR as well as the metal-semiconductor-like transition. More experiments in MoAs₂ such as ARPES need be investigated in future to clarify this phase transition, since it is likely to make out the origin of those transport properties and its topological properties.

Discussion

Presently, the large MR has been discovered and investigated in magnetic multilayers⁵⁷ and semiconductor 2D-electronic systems^{58–61}, in which the rearranged magnetic moments and electron-electron interaction likely play a key role. However, the large unsaturated positive MR recently discovered in some nonmagnetic semimetals^{4,7,27,38} seems to be unique and puzzled. The possible mechanisms can be mainly ascribed to the several factors: (1) the linear energy dispersion of Dirac fermions leading to the quantum limit⁶²; (2) the compensated electron-hole carrier density^{8,26}; (3) the turn on temperature behavior following the Kohler's rule⁴³; (4) other reasons such as protection mechanism³⁸. In MoAs₂, the positive MR shows the almost quadratic field-dependent not

linear at low magnetic fields, implying that the quantum limit should not dominate the transport. MoAs₂ also displays the turn on temperature behavior as $B \geq 5$ T, analogous to the other most of semimetals, but its MR clearly violates the Kohler's rule below 70 K. On the other hand, the sign-changed R_H and the almost equal amount of electron and hole density at low temperatures have been observed in the present sample. We thus suggest that the large MR can be attributed to the electron-hole compensation, similar to WTe₂²⁶.

Unlike the high mobility of the two-dimensional electron gas (GaAs/AlGaAs heterostructure)⁶³, the negative MR associated with the chiral anomaly has been viewed as a key transport signature in semimetal compounds, such as TaSb₂²⁷, TaAs₂³⁰, and Cd₂As₃⁶⁴. When the magnetic field is parallel to the electric current, the chiral anomaly induces the non-conservation of the fermions number with a given chirality, resulting in the negative MR. Recently, an alternative scenario for the negative MR has been suggested, called as the current jetting effect which is associated with an inhomogeneous current distribution inside the sample in a magnetic field^{14,48}. We thus perform the different contact configurations on resistivity measurements (see the Fig. S1 in Supplementary Information). Consequently, the negative MR is robust and shows weakly dependent on the different contact configurations. Therefore, we believed that the current jetting effect may play a minor role in the negative MR in our present sample, as far as in the XPn₂ system^{27,30}.

In summary, we reported an iso-structural MoAs₂ compound which crystallizes in the monoclinic structure with a centrosymmetric space group C2/m. It shows large positive MR and undergoes a metal-semiconductor crossover under 9 T, but clearly violates the Kohler's rule below 70 K. At low temperatures, a robust resistivity plateau with $T_i = 18$ K is observed up to 9 T, which is likely caused by the topological non-trivial surface states whose existence should be further examined by the ARPES experiment. When $B \parallel I$, the negative MR is observed regardless of the different contact configurations, implying a minor current jetting effect in our sample. On the other hand, The analysis of two-band model in Hall resistivity indicates an almost equal amount of electrons and holes at low temperature, consistent with the linear Hall resistivity. A combination of the drop in hole-mobility, the cross point in density and the sign-changed R_H as a function of temperature together with the breakdown of Kohler's rule suggests a possible Lifshitz transition occurring between 30 K and 60 K, likely driving the electron-hole compensation, the large MR as well as the metal-semiconductor-like transition in MoAs₂.

Methods

Very high quality single crystals of monoclinic MoAs₂ were grown through chemical vapor transport reaction using iodine as transport agent. Polycrystalline samples of MoAs₂ were first synthesized by solid state reaction using high purified Tantalum powders and Antimony powders in a sealed quartz tube at 973 K for three days. Subsequently, the final powders together with a transport agent iodine concentration of 10 mg/cm³ were ground thoroughly, and then were sealed in a quartz tube with a low Vacuum-Pressure of $\leq 10^{-3}$ Pa. The single crystals MoAs₂ were grown in a horizontal tube furnace with a temperature gradient of 120 °C between 1120 °C – 1000 °C for 1–2 weeks. The high quality single crystals with apparent monoclinic shape were picked from the resultant.

X-ray diffraction patterns were obtained using a D/Max-rA diffractometer with CuK α radiation and a graphite monochromator at the room temperature. The single crystal X-ray diffraction determines the crystal grown orientation. The composition of the crystals was obtained by energy dispersive X-ray (EDX) spectroscopy. No iodine impurity can be detected in these single crystals. The stoichiometric ratio is fairly homogenous. The (magneto)resistivity and Hall coefficient measurements were performed using the standard four-terminal method in which the current is parallel to the b-axis. Ohmic contacts were carefully prepared on the crystal with a Hall-bar geometry. Silver wires were attached on the surface of crystals with silver paste. The low contact resistance was obtained after annealing at 573 K for an hour. The physical properties were performed in a commercial Quantum Design PPMS-9 system with a torque insert with a temperatures range from 2 to 300 K and the magnetic fields up to 9 T. The density functional theory calculations of MoAs₂ were performed by employing the plane wave basis projector augmented wave (PAW) method implemented in the Vienna ab-initio Simulation Package^{65,66}. The electronic structure calculations were then performed using crystal structures with optimized lattice constants and internal atomic parameters.

References

- Hasan, M. Z. & Kane, C. L. Colloquium: topological insulators. *Rev. Mod. Phys.* **82**, 3045 (2010).
- Wang, Z. J. *et al.* Dirac semimetal and topological phase transitions in A₃Bi (A = Na, K, Rb). *Phys. Rev. B* **85**, 195320 (2012).
- Young, S. M. *et al.* Dirac Semimetal in Three Dimensions. *Phys. Rev. Lett.* **108**, 140405 (2012).
- Liu, Z. K. *et al.* Discovery of a Three-Dimensional Topological Dirac Semimetal, Na₃Bi. *Science* **343**, 864 (2014).
- Jeon, S. *et al.* Landau quantization and quasiparticle interference in the three-dimensional Dirac semimetal Cd₃As₂. *Nat. Mater.* **13**, 851 (2014).
- Neupane, M. *et al.* Observation of a topological 3D Dirac semimetal phase in high-mobility Cd₃As₂. *Nat. Commun.* **5**, 3786 (2014).
- Huang, S. M. *et al.* A Weyl Fermion semimetal with surface Fermi arcs in the transition metal monophosphide TaAs class. *Nat. Commun.* **6**, 7373 (2015).
- Zhang, C. *et al.* Electron scattering in tantalum monoarsenide. *Phys. Rev. B* **95**, 085202 (2017).
- Xu, S. Y. *et al.* Discovery of a Weyl fermion semimetal and topological Fermi arcs. *Science* **349**, 613 (2015).
- Lv, B. Q. *et al.* Experimental discovery of Weyl semimetal TaAs. *Phys. Rev. X* **5**, 031013 (2015).
- Ghimire, N. J. *et al.* Magnetotransport of single crystalline NbAs. *J. Phys.: Condens. Matter* **27**, 152201 (2015).
- Xu, S. Y. *et al.* Discovery of a Weyl fermion state with Fermi arcs in niobium arsenide. *Nat. Phys.* **11**, 748 (2015).
- Shekhar, C. *et al.* Extremely large magnetoresistance and ultrahigh mobility in the topological Weyl semimetal candidate NbP. *Nat. Phys.* **11**, 645 (2015).
- Arnold, F. *et al.* Negative magnetoresistance without well-defined chirality in the Weyl semimetal TaP. *Nat. Commun.* **7**, 11615 (2016).
- Weng, H. *et al.* Weyl semimetal phase in noncentrosymmetric transition-metal monophosphides. *Phys. Rev. X* **5**, 011029 (2015).
- Ren, Z. *et al.* Large bulk resistivity and surface quantum oscillations in the topological insulator Bi_{2+x}Te₂Se. *Phys. Rev. B* **82**, 241306 (2010).

17. Jia, S. *et al.* Defects and high bulk resistivities in the Bi-rich tetradymite topological insulator $\text{Bi}_{2+x}\text{Te}_2\text{Se}$. *Phys. Rev. B* **86**, 165119 (2012).
18. Wolgast, S. *et al.* Low-temperature surface conduction in the Kondo insulator SmB_6 . *Phys. Rev. B* **88**, 180405 (2013).
19. Kim, D. J. *et al.* Surface hall effect and nonlocal transport in SmB_6 : evidence for surface conduction. *Sci. Rep.* **3**, 3150 (2013).
20. Wan, X. *et al.* Topological semimetal and Fermi-arc surface states in the electronic structure of pyrochlore iridates. *Phys. Rev. B* **83**, 205101 (2011).
21. Xu, G. *et al.* Chern semimetal and the quantized anomalous Hall effect in HgCr_2Se_4 . *Phys. Rev. Lett.* **107**, 186806 (2011).
22. Schoop, L. M. *et al.* Dirac cone protected by non-symmorphic symmetry and three-dimensional Dirac line node in ZrSiS . *Nat. Commun.* **7**, 11696 (2016).
23. Hu, J. *et al.* Evidence of topological nodal-line fermions in ZrSiSe and ZrSiTe . *Phys. Rev. Lett.* **117**, 016602 (2016).
24. Sun, Y. *et al.* Prediction of Weyl semimetal in orthorhombic MoTe_2 . *Phys. Rev. B* **92**, 161107 (2015).
25. Wang, Z. J. *et al.* MoTe_2 : a type-II Weyl topological metal. *Phys. Rev. Lett.* **117**, 056805 (2016).
26. Mazhar, N. A. *et al.* Large, non-saturating magnetoresistance in WTe_2 . *Nature* **514**, 205 (2014).
27. Li, Y. K. *et al.* Resistivity plateau and negative magnetoresistance in the topological semimetal TaSb_2 . *Phys. Rev. B* **94**, 121115 (2016).
28. Wang, Y. Y. *et al.* Resistivity plateau and extremely large magnetoresistance in NbAs_2 and TaAs_2 . *Phys. Rev. B* **94**, 041103 (2016).
29. Wu, D. S. *et al.* Giant semiclassical magnetoresistance in high mobility TaAs_2 semimetal. *Appl. Phys. Lett.* **108**, 042105 (2016).
30. Luo, Y. K. *et al.* Anomalous electronic structure and magnetoresistance in TaAs_2 . *Sci. Rep.* **6**, 27294 (2016).
31. Yuan, Z. J. *et al.* Large magnetoresistance in compensated semimetals TaAs_2 and NbAs_2 . *Phys. Rev. B* **93**, 184405 (2016).
32. Shen, B. *et al.* Fermi surface topology and negative longitudinal magnetoresistance observed in the semimetal NbAs_2 . *Phys. Rev. B* **93**, 195119 (2016).
33. Li, Y. P. *et al.* Negative magnetoresistance in topological semimetals of transition-metal dipnictides with nontrivial Z2 Indices. *arXiv* **1603**, 04056 (2016).
34. Wang, K. F. *et al.* Anisotropic giant magnetoresistance in NbSb_2 . *Sci. Rep.* **4**, 7328 (2014).
35. Xu, C. *et al.* Electronic structures of transition metal dipnictides XPn_2 (X = Ta, Nb; Pn = P, As, Sb). *Phys. Rev. B* **93**, 195106 (2016).
36. Taylor, J. B., Calvert, L. D. & Hunt, M. R. The arsenides of tungsten and molybdenum: WAs_3 , W_2As_3 , MoAs_3 , Mo_2As_3 , and Mo_3As_4 . *Canadian Journal of Chemistry* **43**, 3045 (1965).
37. Jensen, P. & Kjekshus, A. The Crystal Structure of Mo_3As_4 . *Acta Chemica Scandinavica* **18**, 1798 (1966).
38. Liang, T. *et al.* Ultrahigh mobility and giant magnetoresistance in the Dirac semimetal Cd_3As_2 . *Nat. Mater.* **14**, 280 (2015).
39. Ali, M. N. *et al.* Butterfly magnetoresistance, quasi-2D Dirac Fermi surface and topological phase transition in ZrSiS . *arXiv* **1603**, 09318 (2016).
40. Alers, P. B. & Webber, R. T. The magnetoresistance of bismuth crystals at low temperatures. *Phys. Rev.* **91**, 1060 (1953).
41. Ziman, J. M. *Electrons and Phonons, Classics Series* (Oxford: Oxford University Press) (2001)
42. Ahn, K. H. *et al.* Magnetic properties and colossal magnetoresistance of $\text{La}(\text{Ca})\text{MnO}_3$ materials doped with Fe. *Phys. Rev. B* **54**, 15299 (1996).
43. Thoutam, L. R. *et al.* Origin of the turn-on temperature behavior in WTe_2 . *Phys. Rev. Lett.* **115**, 046602 (2015).
44. Clarke, D. G. *et al.* The quantum-classical metal. *Science* **279**, 2071 (1998).
45. Ando, Y. & Segawa, K. Electrical resistivity anisotropy from self-organized one dimensionality in high-temperature superconductors. *Phys. Rev. Lett.* **88**, 167005 (2002).
46. Tafti, F. F. *et al.* Resistivity plateau and extreme magnetoresistance in LaSb . *Nat. Phys.* **12**, 272 (2016).
47. Zeng, M. *et al.* Topological semimetals and topological insulators in rare earth monopnictides. *arXiv*: 1504.03492 (2015)
48. Reis, R. Ddos *et al.* On the search for the chiral anomaly in Weyl semimetals: The negative longitudinal magnetoresistance. *New J. Phys.* **18**, 085006 (2016).
49. Chang, M. C. & Yang, M. F. Chiral magnetic effect in the absence of weyl node. *Phys. Rev. B* **92**, 205201 (2015).
50. Ma, J. & Pesin, D. A. Chiral magnetic effect and natural optical activity in metals with or without weyl points. *Phys. Rev. B* **92**, 235205 (2015).
51. Fu, L. & Kane, C. L. Topological insulators in three dimensions. *Phys. Rev. B* **76**, 045302 (2007).
52. Wu, Y. *et al.* Temperature-induced Lifshitz transition in WTe_2 . *Phys. Rev. Lett.* **115**, 166602 (2015).
53. Pletikosi, I. *et al.* Electronic structure basis for the extraordinary magnetoresistance in WTe_2 . *Phys. Rev. Lett.* **113**, 216601 (2014).
54. Dai, Y. M. *et al.* Ultrafast carrier dynamics in the large-magnetoresistance material WTe_2 . *Phys. Rev. B* **92**, 161104 (2015).
55. Zhou, Q. *et al.* Hall effect within the colossal magnetoresistive semimetallic state of MoTe_2 . *Phys. Rev. B* **94**, 121101 (2016).
56. Luo, Y. K. *et al.* Hall effect in the extremely large magnetoresistance semimetal WTe_2 . *Appl. Phys. Lett.* **107**, 182411 (2015).
57. Salamon, M. B. & Jaime, M. The physics of manganites: Structure and transport. *Rev. Mod. Phys.* **73**, 583 (2001).
58. Bockhorn, L. *et al.* Magnetoresistance in a high-mobility two-dimensional electron gas. *Phys. Rev. B* **83**, 113301 (2011).
59. Wang, Z. *et al.* Tunable electron heating induced giant magnetoresistance in the high mobility $\text{GaAs}/\text{AlGaAs}$ 2D electron system. *Sci. Rep.* **6**, 38515 (2016).
60. Samaraweera, R. L. *et al.* Mutual influence between current-induced giant magnetoresistance and radiation-induced magnetoresistance oscillations in the $\text{GaAs}/\text{AlGaAs}$ 2DES. *Sci. Rep.* **7**, 5074 (2017).
61. Mani, R. G., Kriisa, A. & Wegscheider, W. Size-dependent giant-magnetoresistance in millimeter scale $\text{GaAs}/\text{AlGaAs}$ 2D electron devices. *Sci. Rep.* **3**, 2747 (2013).
62. Abrikosov, A. A. Quantum magnetoresistance. *Phys. Rev. B* **58**, 2788 (1988).
63. Hatke, A. T. *et al.* Giant negative magnetoresistance in high-mobility two-dimensional electron systems. *Phys. Rev. B* **85**, 081304 (2012).
64. Li, C. Z. *et al.* Giant negative magnetoresistance induced by the chiral anomaly in individual Cd_3As_2 nanowires. *Nat. Comm.* **6**, 10137 (2015).
65. Kresse, G. & Hafner, J. Ab initio molecular dynamics for liquid metals. *Phys. Rev. B* **47**, 558 (1993).
66. Kresse, G. & Joubert, D. From ultrasoft pseudopotentials to the projector augmented-wave method. *Phys. Rev. B* **59**, 1758 (1999).

Acknowledgements

This research was supported in part by the NSF of China (under Grants No. 11274006 and No. 11274084) and the National Basic Research Program (under Grant No. 2014CB648400). Yu-Ke Li was supported by an open program from Wuhan National High Magnetic Field Center (2016KF03). We would like to thank Yi Liu, Jianhua Du and Qunlin Ye for technique assistances. The authors are grateful to Hangdong Wang, Shiyang Li for stimulating discussions.

Author Contributions

Y. Li designed the research. J. Wang synthesized the samples. J. Wang and Y. Li performed most measurements. L. Li, W. You and T. Wang assisted the measurements. C. Cao performed the band structure calculations. J. Dai, and Y. Li, discussed the data, interpreted the results, and wrote the paper.

Additional Information

Supplementary information accompanies this paper at <https://doi.org/10.1038/s41598-017-15962-w>.

Competing Interests: The authors declare that they have no competing interests.

Publisher's note: Springer Nature remains neutral with regard to jurisdictional claims in published maps and institutional affiliations.



Open Access This article is licensed under a Creative Commons Attribution 4.0 International License, which permits use, sharing, adaptation, distribution and reproduction in any medium or format, as long as you give appropriate credit to the original author(s) and the source, provide a link to the Creative Commons license, and indicate if changes were made. The images or other third party material in this article are included in the article's Creative Commons license, unless indicated otherwise in a credit line to the material. If material is not included in the article's Creative Commons license and your intended use is not permitted by statutory regulation or exceeds the permitted use, you will need to obtain permission directly from the copyright holder. To view a copy of this license, visit <http://creativecommons.org/licenses/by/4.0/>.

© The Author(s) 2017